RSC Advances

PAPER

View Article Online
View Journal | View Issue

Cite this: *RSC Adv.*, 2022, **12**, 2150

Enhancing adsorption capacity and structural stability of $Li_{1.6}Mn_{1.6}O_4$ adsorbents by anion/cation co-doping†

Yifan Su,[ab] Fangren Qian[ab] and Zhiqiang Qian *[ab]

Modifying the structure of $Li_{1.6}Mn_{1.6}O_4$ (LMO) to enhance its structural stability and adsorption capacity is an effective method to generate materials to recover Li^+ ions from mixed solution. Herein, the co-doping of trace non-metal ion (S) and metal ion (Al) into $Li_{1.6}Mn_{1.6}O_4$ (LMO-SAl) is established and shows excellent Li^+ adsorption capacity and Mn anti-dissolution properties. The adsorption capacity (when $[Li^+]$ is 6 mmol L^{-1}) is increased from 26.1 mg g^{-1} to 33.7 mg g^{-1}. This is attributed to improved charge density *via* substitution of S at O sites, which facilitates the adsorption/desorption process. The Mn dissolution is also reduced from 5.4% to 3.0% for LMO-SAl, which may result from the stronger Al–O bonds compared to Li–O bonds that enhance the structural stability of the LMO. The ion-sieving ability of the co-doped material goes by the order of K_d ($Li^+ > Ca^{2+} > Mg^{2+} > Na^+ > K^+$), indicating that Li^+ can be efficiently separated from Lagoco Salt Lake brine. These results predict that lithium ions are effectively adsorbed from brine by the co-doped LMO material, which manifests the feasibility of lithium recovery and provides basic data for further industrial applications of adsorption.

Received 19th October 2021
Accepted 6th January 2022

DOI: 10.1039/d1ra07720a

rsc.li/rsc-advances

1. Introduction

Due to the production of ceramics, glass, grease, and especially lithium batteries, the demand for lithium (Li) and its compounds continues to increase.[1] Salt lakes and seawater are regarded as vital sources of lithium, however, it is difficult to recover Li^+ ions from the mixed solution because of the low concentrations of Li^+ and the high quantity of co-existing ions such as Na^+, K^+, Mg^{2+}, and Ca^{2+}.[2] Numerous technologies have been adopted to extract lithium, including solvent extraction,[3] membrane technology[4] and adsorption,[5] however, using highly selective adsorption has been identified as one of the most promising and environmentally friendly technologies for Li^+ recovery from low-concentration solutions.

For the recovery of Li^+ ions from salt lakes or seawater using ion-exchange adsorption technology, the key step is to prepare adsorbents with high Li^+ adsorption capacities and low manganese (Mn) dissolution. As lithium ion-sieves, manganese oxides with spinel structure, including $LiMn_2O_4$,[6] $Li_4Mn_5O_{12}$,[7] and $Li_{1.6}Mn_{1.6}O_4$,[8] have excellent adsorption characteristics due to their unique pores. Especially, $Li_{1.6}Mn_{1.6}O_4$ (LMO) has the highest theoretical Li^+ absorption, but there will still be undesirable Mn loss during acid treatment, which hinders its further application in industry.[9] Many methods including element doping,[10] surface coating[11] and electrochemical ion-separation[12] have been used to improve the stability of LMO. Foreign element doping is considered one of the most effective technologies to enhance the regeneration ability of $Li_{1.6}Mn_{1.6}O_4$. Many studies have explored the influence of doping elements (such as Al, Fe, Mg, and Ni) on the structural stability of LMO.[13–16] Among them, many studies have tried to use metal ion doping to improve the cycle stability of $Li_{1.6}Mn_{1.6}O_4$. Nevertheless, there are few studies on anion doping, and almost no studies on anion and cation co-doping. However, co-doping is expected to further improve the structural stability by adjusting the electronic structure.[17]

In general, it is difficult to improve the adsorption capacity and reduce the Mn dissolution loss of $Li_{1.6}Mn_{1.6}O_4$ simultaneously by single ion doping. In our previous works, it was found that cation doping reduces the dissolution loss of Mn, and anion doping increases the adsorption capacity of Li^+.[5,8,9] However, cation and anion co-doped LMO are still a virgin field for exploration, which is considered to further improve structural stability and Li^+ uptake capacities by tailoring the electronic structure and synergistic effect. Most often, S ion provide more charge carriers than O ion,[9] and Al ions can enhance the Mn anti-dissolution more than Li ions in LMO.[5] In general, these two properties are difficult to improve simultaneously by single ion doping. In this work, $Li_{1.6}Mn_{1.6}O_4$ with non-metal ion (S) and metal ion (Al) co-doped was synthesized, and the

[a]*Key Laboratory of Comprehensive and Highly Efficient Utilization of Salt Lake Resources, Qinghai Institute of Salt Lakes, Chinese Academy of Sciences, Xining, Qinghai 810008, China. E-mail: qianzq@isl.ac.cn*

[b]*Qinghai Provincial Key Laboratory of Resources and Chemistry of Salt Lake, Xining, Qinghai 810008, China*

† Electronic supplementary information (ESI) available. See DOI: 10.1039/d1ra07720a

morphology and microstructure were characterized using various techniques. The adsorption/desorption properties of co-doping with anions (S) and cations (Al) were systematically investigated. It is indicated that a vital improvement was demonstrated in the logical design and preparation of anions and cations co-doped in $Li_{1.6}Mn_{1.6}O_4$ to enhance the adsorption and anti-dissolution properties.

2. Materials and methods

2.1 Preparation of doped materials

To begin, a hydrothermal process was used to produce orthorhombic $LiMnO_2$.[18] The co-doped samples were prepared by calcinating mixtures of $(NH_4)_2S$ and $AlCl_3$ with $LiMnO_2$ at a certain molar ratio at 350 °C for 24 h to form LMO-SAl. The ion-sieve (HMO-SAl) was obtained by the HCl (0.6 mol L^{-1}) treatment of precursor (LMO-SAl) at 25 °C with magnetic stirring for 24 h. The samples are expressed as r-LMO-SAl. In addition, samples doped with a single S (derived from $(NH_4)_2S$, designated as LMO-S, HMO-S, and r-LMO-S), or a single Al (derived from $AlCl_3$, denoted as LMO-Al, HMO-Al, and r-LMO-Al), and samples without doping (designated as LMO, HMO and r-LMO) were prepared by the above-mentioned method.

2.2 Sample characterization

The crystalline phases were characterized by X-ray diffraction (XRD, X-Pert PRO), and the scanning angle 2θ range is 10–90°. The morphologies of as-obtained samples were analyzed by a scanning electron microscope (SEM, LEO 1530VP). Through X-ray photoelectron spectroscopy (XPS, ESCALAB 250Xi), the surface content and binding energy changes were investigated. The Mn^{4+} and Li^+ concentrations in the solution was measured using an inductively coupled plasma emission spectrometer (ICP-OES, Optima 7000DV). The functional groups were recorded by Fourier transform infrared spectroscopy (FT-IR spectroscopy, Bruker Tensor 27), in the range of 400 to 4000 cm^{-1}.

2.3 Li^+ adsorption properties

The Li^+ adsorption/desorption process by LMO-SAl are illustrated in Fig. 1. The batch experiments for the adsorption of Li^+ in solution were carried out in a thermostatic water bath with a shaking speed of 150 rpm for 48 h. In a typical batch experiment, 0.1 g of HMO-SAl was put into 100 mL of LiCl solution. The influence of factors (such as solution pH, experiment temperature, initial solution concentration) on the adsorption capacity of adsorbent were investigated. The solution pH values were adjusted over the range of 4–12 using by HCl or NaOH solution, the initial Li^+ concentration was 6, 8, 12, 24, or 36 mmol L^{-1}, and the temperature range of the experiments was 25–45 °C.

The equilibrium adsorption (q_e) was calculated using the following eqn (1):[19]

$$q_e = \frac{V}{m}(C_0 - C_e) \quad (1)$$

where q_e represents the Li^+ adsorption uptake (mg g^{-1}); C_0 and C_e signify the initial and final Li^+ concentrations in the solution (mg L^{-1}); m is the weight of the HMO-Al-R (g); and V is the solution volume (L).

The adsorption selectivity was determined in a MCl (M^+ = Li^+, Na^+, K^+, Rb^+, Cs^+) mixture solution. To evaluate the adsorption behaviors of the prepared adsorbents under Salt Lake brine, 0.1 g of HMO-SAl was added to the Lagoco Salt Lake brine (100 mL). The distribution coefficient (K_d), concentration factor (C_F), and separation factor (α_M^{Li}) were obtained by eqn (2)–(4), respectively.[20]

$$K_d = (C_0 - C_e)\frac{V}{mC_e} \quad (2)$$

$$C_F = q_{e_M}/C_{0_M} \quad (3)$$

$$\alpha_M^{Li} = \frac{K_{Li}}{K_d} \quad (4)$$

2.4 Dissolution of Mn

The Mn content in the solid adsorbent is obtained by dissolving LMO-SAl in a mixed solution containing HCl/H_2O_2 and measuring the concentration of Mn in the solution. The Mn dissolution rates was obtained by eqn (5):[21]

$$r = C_i/S \quad (5)$$

where r is the rate of dissolved Mn; C_i refers to the Mn^{2+} concentration in the solution at a certain time; S is the content of Mn^{2+} in the adsorbent.

2.5 DFT calculations

The structure and electronic properties of the LMOs were investigated using first-principles calculations with DFT, implemented using the Vienna *Ab initio* Simulation Package (VASP)[18] Our previous work established the correlation methods and parameter settings.[19] The ESI† includes detailed information about the calculation.

3. Results and discussion

3.1 Preparation of co-doping LMO

The XRD patterns of co-doping LMO/HMO are shown in Fig. 2. It is indicated that the diffraction peaks for the precursors (LMOs), ion-sieves after HCl treatment (HMOs), and materials with Li^+ reinserted by co-doping (r-LMOs) correspond to a spinel structure. The interplanar spacing decreases from 4.7 Å to 4.6 Å after the acid leaching process, and return to 4.7 Å after Li^+ reinsertion, implying that the structure is stable in both acidic and alkaline environments and that ion-exchange occurs *via* an adsorption/desorption process.[22] The morphologies of as-prepared samples are shown in Fig. 3a–c. It can be indicated that the morphology of co-doped LMO and HMO changes little in an acidic or alkaline environment. The EDS element mapping shows that the elements (O, Mn, S, Al) are uniformly distributed (Fig. 3e).

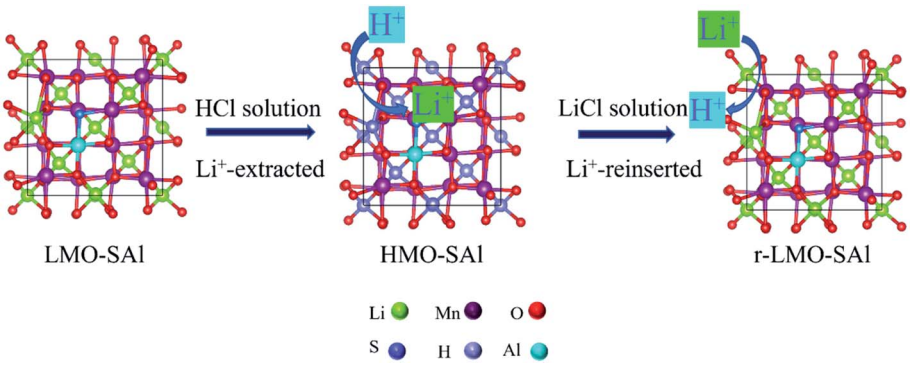

Fig. 1 Schematic illustration of the LMO-SAl for Li^+ adsorption and desorption process.

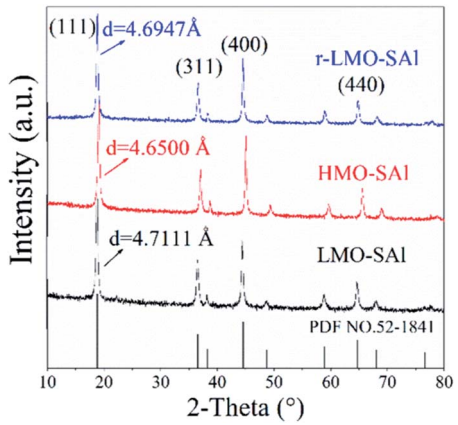

Fig. 2 The XRD patterns of various manganese oxides with co-doping (the precursors (LMOs), ion-sieves after HCl treatment (HMOs), and materials with Li^+ reinserted by co-doping (r-LMOs)).

The FT-IR spectra of the co-doped anions and cations LMO and HMO are shown in Fig. 4. The –OH bands near 3422 cm^{-1} and 1628 cm^{-1} are existed in the spectrum of the co-doped LMO, however the intensity of the –OH signal is enhanced in the co-doped HMO, which means that the ion exchange between Li^+ and H^+ occurs in Li^+ extraction process.[23] In addition, a new peak near 907 cm^{-1} appeared in the HMO-SAl sample, which further supports the existence of the ion exchange process.[23] The peak near 1072 cm^{-1} in the LMO-SAl sample is attributable to the Li–O bond, which is still existed in the HMO-SAl sample, but the peak intensity decreases, indicating that the Li^+ desorption is incomplete, which may be due to the Li^+ in the 16d site is difficult to extract.[24] The bands of Mn(III)–O and Mn(IV)–O are similar in the co-doping LMO and HMO, demonstrating that the spinel structure has high stability in acidic environment,[25] which is consistent with the XRD results.

Fig. 5 shows the XPS fitting curve of the co-doped LMO and HMO. There are [Mn^{4+}O] bands at 642.7 eV and [Mn^{3+}O] bands close to 642.1 eV in the spectra of co-doped LMO and HMO,[26] while the amount of Mn^{4+} in HMO is higher because Mn^{3+} is partially dissolved in HCl solution (Fig. 5a). Compared with the LMO (Fig. S1†), the amount of Mn^{4+} is increased (84%) by co-doping, which improves the resistance to solubility. After Li^+ is extracted, the –OH band intensity near 531 eV increases,[27] while the peak caused by [MnO_6] does not change in the co-doped LMO and HMO (Fig. 5b), indicating that during the Li^+/H^+ ion exchange process, the framework structure of [MnO_6] shows stable in an acidic environment, which is consistent with the results of FT-IR.[28]

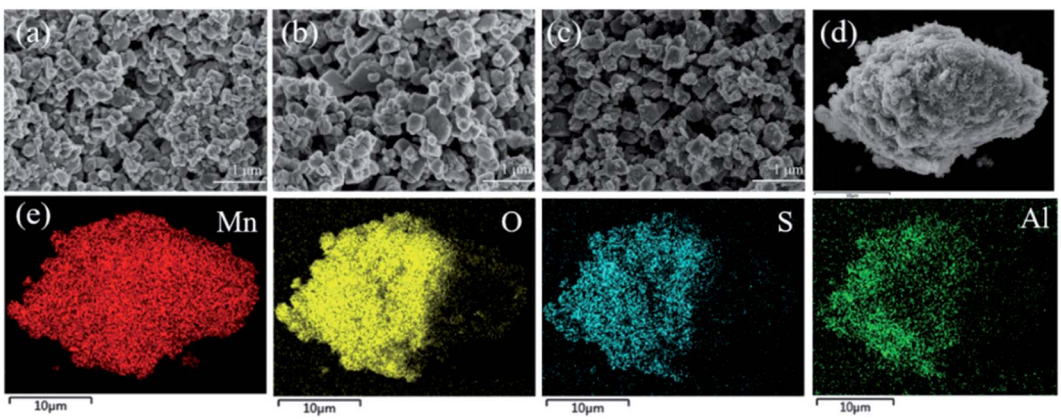

Fig. 3 Morphologies of (a) LMO-SAl; (b) HMO-SAl (c) r-LMO-SAl and (d) enlarged of LMO-SAl; (e) are the elemental mapping from EDS and survey spectra of EDS from (d), respectively.

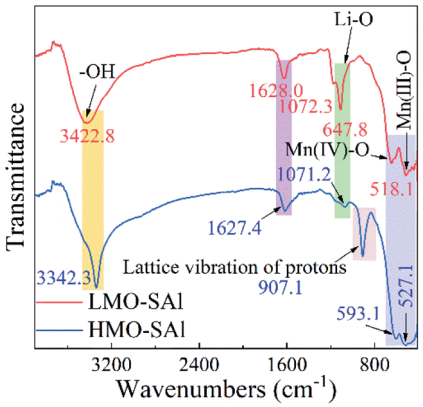

Fig. 4 FT-IR spectra of co-doped LMO (LMO-SAl) and co-doped HMO (HMO-SAl).

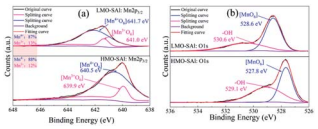

Fig. 5 XPS spectra of different LMO-SAl and HMO-SAl. (a): Mn 2p and (b) O 1s fitting curves.

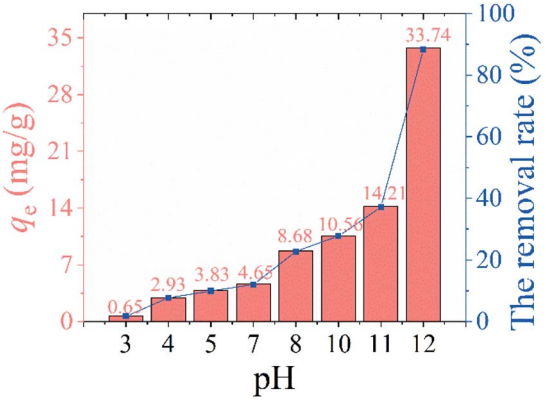

Fig. 6 The adsorption capacity and removal rate of HMO-SAl at various pH (3–12).

3.2 Adsorption properties

3.2.1 Effect of pH. Fig. 6 shows the effect of solution pH on lithium adsorption. The effect of solution pH on the lithium adsorption is shown in Fig. 6. The Li^+ adsorption capacity of HMO-SAl is extremely low (<5 mg g^{-1}) in an acidic environment. The adsorption of HMO-SAl increased to 10.56 mg g^{-1} at pH 10, and reached 33.74 mg g^{-1} at pH 12. It can be considered that the adsorption capacity increases with the increase of pH, which may be due to the promotion of the ion exchange process by the alkaline environment according to eqn (6).[29]

$$H_{1.6}Mn_{1.6}O_4 + Li \rightleftharpoons Li_{1.6}Mn_{1.6}O_4 + H \quad (6)$$

3.2.2 Influence of initial Li^+ concentration and temperature. Fig. 7 shows the adsorption of the adsorbent in different LiCl solution concentrations and different temperatures. It can be seen from Fig. 7a that the adsorption capacity of HMO increases with the increase of the initial concentration. When C_{LiCl} = 6 mmol L^{-1}, the equilibrium adsorption capacity of HMO-SAl is 33.7 mg g^{-1}. As the concentration of LiCl solution increases to 24 mmol L^{-1}, its adsorption capacity increases to 40.4 mg g^{-1}. It can be considered that the adsorption capacity increases with the increase of the initial lithium concentration, and the adsorption capacity of co-doped HMO increases significantly compared with un-doped HMO (Fig. S3,† 22.5 mg g^{-1} at C_{LiCl} = 6 mmol L^{-1}). In addition, the adsorption capacity of HMO-SAl is also higher than HMO-Al (29.4 mg g^{-1}) and HMO-S (27.4 mg g^{-1}). The reason may be the synergistic effect of the replacement of anion and cation, which improves the structural stability and inhibits the irreversible capacity decay caused by the Jahn–Teller effect.[15]

Fig. 7b shows the adsorption of Li^+ by the HMO-SAl at different temperatures. The adsorption capacity of HMO-SAl at 25 °C is 33.7 mg g^{-1}. When the temperature continues to increase to 35 °C and 45 °C, the adsorption capacity increases to 34.4 mg g^{-1} and 36.2 mg g^{-1}, respectively. The results show that as the temperature increases, the equilibrium adsorption capacity also increases, indicating that the adsorption of Li^+ by HMO-SAl is an endothermic reaction.

The performance of the element doping in Li–Mn–O ionic sieves have been summarized in Table S1.† Overall, the proposed HMO-SAl material demonstrated a higher adsorption capacity at a relatively low initial Li^+ concentration than has been shown in prior works, as summarised in Table S1 in ESI.† This anion/cation co-doping HMO in the present work has excellent uptake properties and may have a promising application for the recovery of Li^+ from solution containing Li^+.

3.2.3 Adsorption isotherms. The Langmuir and Freundlich adsorption isotherm models are used to investigated the absorption behavior of Li^+, which can be shown as eqn (7) and (8):[30]

$$\frac{C_e}{q_e} = \frac{1}{q_m b} + \frac{C_e}{q_m} \quad (7)$$

$$\ln q_e = \ln k_F + \frac{1}{n} \ln C_e \quad (8)$$

where C_e means the equilibrium concentration of Li^+ (mg L^{-1}), q_e and q_m are the experimental and theoretical capacities (mg g^{-1}), b, k_F (mg g^{-1}) and n denote is the Langmuir coefficient and the Freundlich constants, respectively.

Fig. 8 shows the fitting curve, and the relevant parameters are listed in Table 1. It can be observed that the Li^+ adsorption behavior is fit better to a Langmuir model (R^2 = 0.99) than a Freundlich model (R^2 = 0.86), which is indicated that it is a single layer adsorbed to the surface.[30]

3.2.4 Adsorption kinetics. The pseudo-first order, pseudo-second order, and intraparticle diffusion model are employed

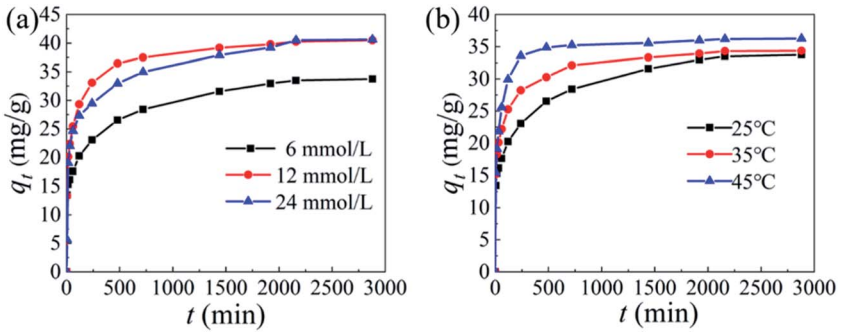

Fig. 7 The adsorption capacity of HMO-SAl: (a) various initial adsorption concentration (6 mmol L^{-1}, 12 mmol L^{-1} and 24 mmol L^{-1}), (b) various temperature (25 °C, 35 °C and 45 °C).

to investigate the adsorption kinetics of Li^+. The equations are shown as follows:[31]

$$\ln(q_e - q_t) = \ln q_e - k_1 t \quad (9)$$

$$\frac{t}{q_t} = \frac{1}{k_2 q_e^2} + \frac{t}{q_e} \quad (10)$$

$$q_t = k_n t^{0.5} + C_n \quad (11)$$

where q_e and q_t are the Li^+ adsorption capacities (mg g^{-1}) at equilibrium and random time t (min), the k_1 (min^{-1}) and k_2 (g (mg^{-1} min^{-1})) signify pseudo-first-order and pseudo-second-order coefficients, and k_n (mol g^{-1} $min^{-0.5}$) denotes the diffusion rate coefficient of process n (n = 1, 2, 3).

The fitting results are shown in Fig. 9, and the relevant parameters are summarized in Table 2. Comparing to the pseudo-first-order (R^2 = 0.98), the R^2 (0.99) of pseudo-second-order of HMO-SAl adsorbents is closer to linear, and a $q_{e,cal}$ based on a pseudo-second-order model is closer to $q_{e,exp}$, which is indicated that the pseudo-second-order model is more in line with the adsorption process of Li^+, suggesting the Li^+ absorption is mainly promoted by the chemical adsorption caused by the ion exchange between Li^+ and H^+.

The model of the particle internal diffusion was investigated, and the diffusion rate constants (k_n) were calculated. The fitted line is shown in Fig. 9c. It can be seen from Fig. 9c that the first process fitting line has a steep slope, which indicates that Li^+ is transferred from the solution to the surface of the adsorbent during the rate control process. The slope of the second segment of the fitted line gradually plateaus, indicating that a decelerating adsorption process has occurred during this process, in which Li^+ may migrate from the surface to the pores. In the third step, the transfer of Li^+ inside the particle slows down, indicating that the absorption has reached equilibrium.[30]

3.2.5 Adsorption selectivity. The presence of coexisting ions has a significant impact on the absorption behavior of Li^+ in low-concentration Li solutions (such as salt lakes).

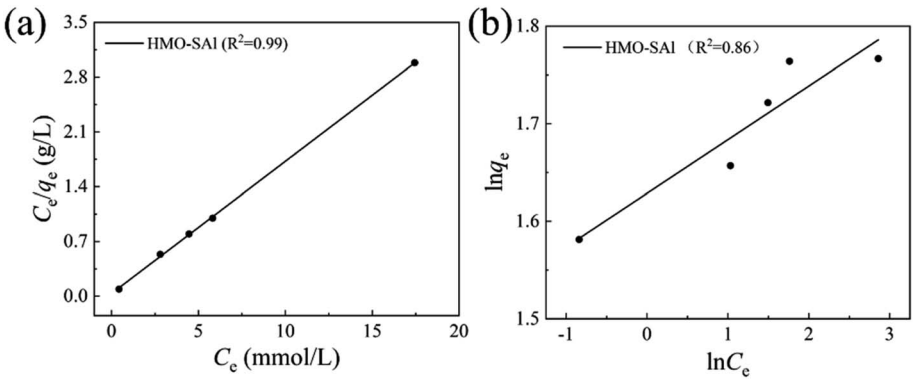

Fig. 8 (a) Langmuir, (b) Freundlich isotherm models of Li^+ uptake behavior of HMO-SAl. (T = 25 °C, C_{Li^+} = 6 mmol L^{-1}).

Table 1 Relevant parameters base on Langmuir and Freundlich models (T = 25 °C)

	Langmuir			Freundlich		
Material	q_m (mg g^{-1})	b (L mg^{-1})	R^2	k_F (mg g^{-1}) (L mg^{-1})$^{1/n}$	n	R^2
HMO-SAl	41.08	5.02	0.99	4.04	18.18	0.86

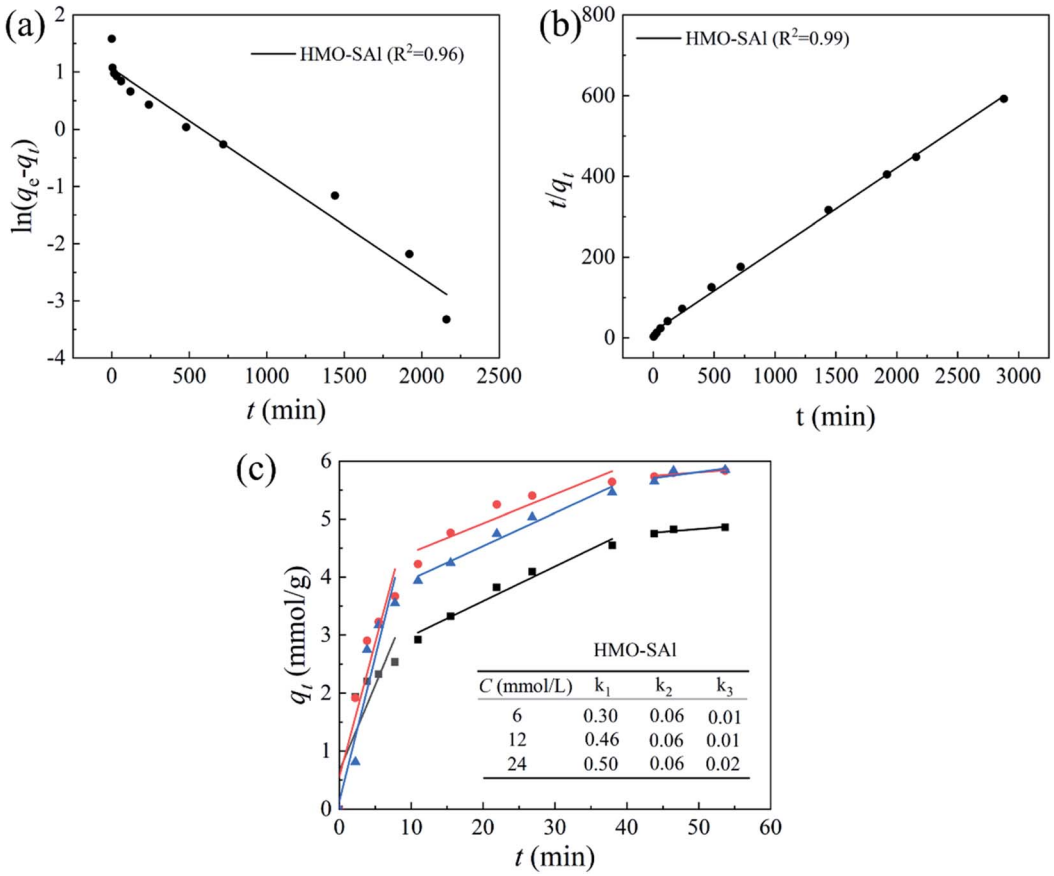

Fig. 9 (a) Pseudo first-order; (b) pseudo-second-order and (c) intra particle diffusion models for Li^+ uptake behavior (T = 25 °C C_{Li^+} = 6 mmol L^{-1}).

Table 2 Relevant parameters base on kinetics models (T = 25 °C)

		Pseudo-first-order			Pseudo-second-order		
Materials	$q_{e,exp}$ (mg g^{-1})	k_1 (min^{-1})	$q_{e,cal}$	R^2	k_2 (min^{-1})	$q_{e,cal}$ (mg g^{-1})	R^2
HMO-SAl	33.74	0.002	12.29	0.96	0.003	34.19	0.99

The adsorption curves of ions for HMO-SAl adsorbents in single and mixed MCl solutions are shown in the Fig. 10. In a single LiCl solution, the absorption capacity of HMO-SAl for Li^+ is 4.86 mmol g^{-1}, which is higher than that of the mixed solution (4.58 mmol L^{-1}). However, HMO-SAl hardly adsorbs other ions, which may be because the pore size of the adsorbent is similar to the ion radius of Li^+, while other ions with a larger radius cannot enter the pores and are adsorbed on the surface.[30] In particular, the absorption capacity of HMO-SAl in a single LiCl solution or mixed solution is higher than single ion doped HMO (HMO-Al and HMO-S).[5,9]

In order to evaluate the practicality of the HMO-SAl adsorbent, adsorption experiments were carried out in Lagoco Salt Lake brine containing Mg^{2+} and Ca^{2+}, and the results are summarized in Table 3. The absorption results show that HMO-SAl has high selectivity to Li+ (Li^+> Ca^{2+}> Mg^{2+}> Na^+> K^+) according to the order of K_d in Table 3, which means that the

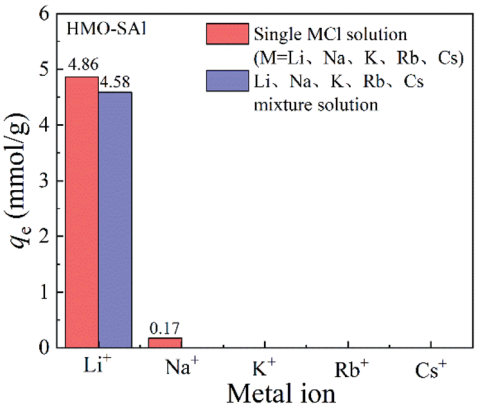

Fig. 10 Adsorption capacity of HMO-Al-5% for various monovalent cations in single and mixed MCl solutions.

Table 3 Selectivity of HMO-SAl in Lagoco salt lake

Ions	C_0 (mmol L^{-1})	C_e (mmol L^{-1})	q_e (mmol g^{-1})	C_F (mL g^{-1})	K_d (mL g^{-1})	$\alpha_{Li/M}$
Li^+	45.18	41.00	4.18	92.52	101.95	1
Na^+	723.99	723.97	0.02	0.03	0.03	3398.33
K^+	63.53	63.50	0.03	0.47	0.47	216.91
Mg^{2+}	35.75	35.73	0.02	0.56	0.56	182.05
Ca^{2+}	0.41	0.41	0.001	2.44	2.44	41.78

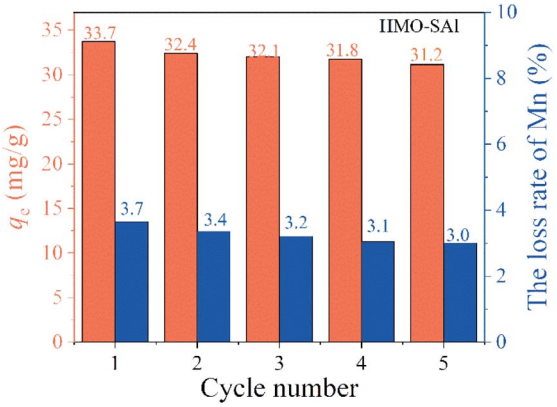

Fig. 11 Li^+ uptake and Mn loss rate of HMO-SAl in regeneration process.

material has the ability to separate Li^+ from solutions containing Mg^{2+} and Ca^{2+}. The all separation factors (α_M^{Li}) of HMO-SAl greatly exceed those of HMO-Al, suggesting that HMO-SAl possess excellent and effective separation effect. The results show that HMO-SAl has high selectivity to Li^+ from Lagoco Salt Lake brine, which has broad application prospects for Li^+ recovery.

3.2.6 Cyclic adsorption performance. The absorption of Li^+ and the dissolution loss of Mn in the five cycles of adsorption and desorption of HMO-SAl are shown in Fig. 11.

It can be clearly noticed that during the initial regeneration process, the adsorption of Li^+ and the loss of Mn are significantly reduced, which can be attributed to the presence of $LiMnO_2$.[32] After the fifth cycle, the Li^+ absorption capacity of HMO-SAl is 93% of the first adsorption capacity. Compared with the adsorption capacity of HMO-Al (28.0 mg g^{-1}) after five adsorptions, the adsorption capacity of HMO-SAl increased by 11.4%. Correspondingly, the dissolution loss rate of Mn is below 3.0%, indicating that HMO-SAl has excellent adsorption performance and stable structure.

3.3 Dissolution loss of Mn

The dissolution loss of Mn with different concentrations of hydrochloric acid and different temperatures is shown in Fig. 12. The solubility of Mn increased slightly from 2.9% to 3.0% as the HCl concentration increased from 0.3 mol L^{-1} and 0.6 mol L^{-1} respectively, which are slightly higher than the dissolution loss of HMO-Al. Fig. 12b shows that the Mn dissolution rate increases with increasing temperature. This means that in an acidic environment, the dissolution rate of Mn increases, which may be stimulated by eqn (12):[33]

$$4(Li)[Mn(III)]O_4 + 8H \rightarrow 3(\square)[Mn_2(IV)O_4] + 4Li^+ + 2Mn(II) + 4H_2O \quad (12)$$

Among them, "□" signifies an unoccupied Li^+.

3.4 Enhanced adsorption and anti-dissolution properties

A comparison of the adsorption capacity and Mn loss rate of bare LMO, single doped LMO, and co-doped LMO are illustrated in Fig. 13. The adsorption capacity of HMO-SAl is 33.7 mg g^{-1},

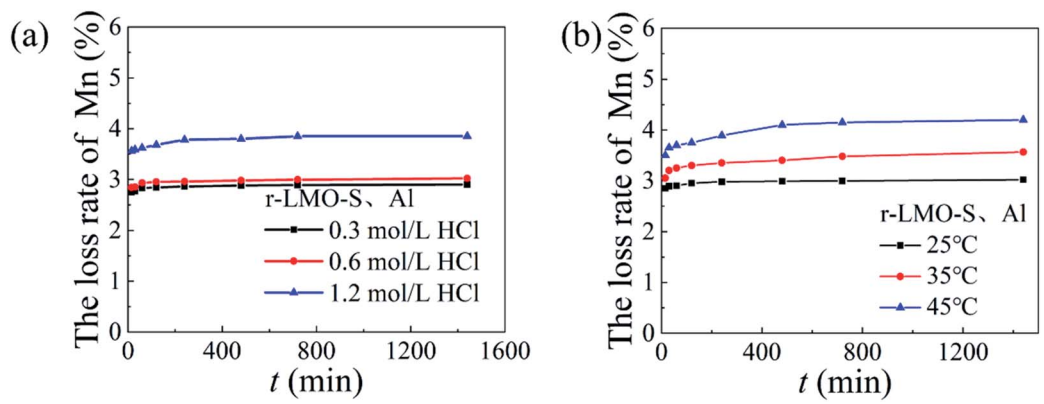

Fig. 12 The Mn loss rate of HMO-SAl: (a) various HCl concentration (T = 25 °C), (b) various temperature (c_{HCl} = 0.6 mol L^{-1}).

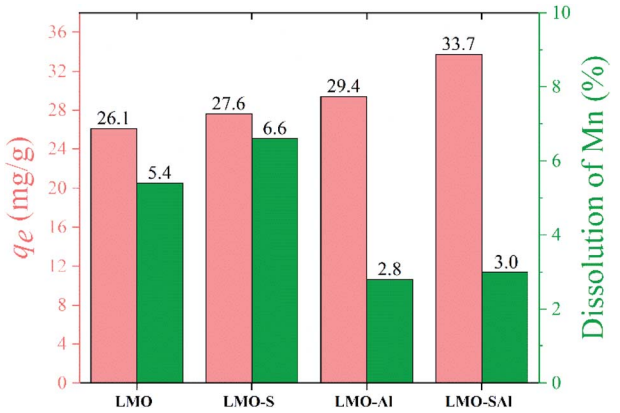

Fig. 13 Comparison of Li^+ adsorption capacity and Mn dissolution of un-doped LMO, S dpoed LMO, Al doped LMO and co-doped LMO.

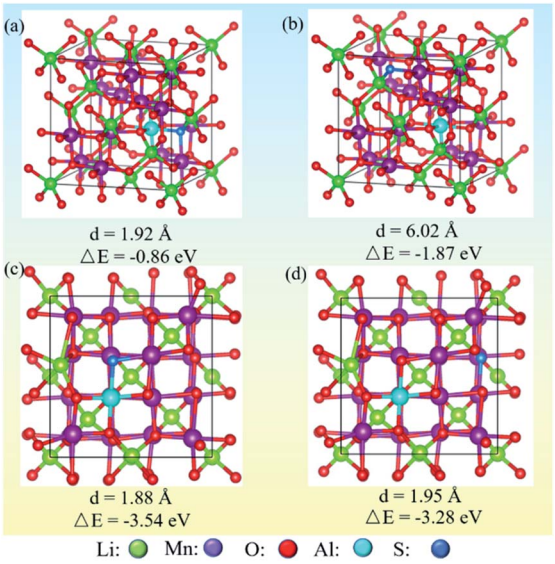

Fig. 14 Optimized structures of replacing Li and O sites with anions (S) and cation (Al). (a and b) Near and far S–Al in bulk; (c and d) near and far S–Al in surface.

which is higher than both the bare HMO and single Al doped (HMO-Al), and slightly lower than single S doped (HMO-S). The Mn dissolution decreased to 3.7% in S and Al co-doped (HMO-SAl), which is lower than bare LMO (5.4%), LMO-S (5.4%), and LMO-Al (4.4%), indicating that the S and Al co-doped can effectively reduce the Mn dissolution and improve the Li^+ adsorption. These may be caused by an improvement in the charge density produced by S doping. The impact of Al doping may be due to its ability to reinforce the structural stability of the LMOs, in alignment with our previous work. In summary, both anions and cations co-doped can enhance the adsorption and anti-dissolution properties.[10]

3.5 Theory calculations

3.5.1 Anion and cation co-doping induced structure stability. Theory calculations were performed to probe the surface structure of co-doped LMOs. To illustrate the formation of surface doped structures when anions and cations were substituted, the energies of different models were calculated. The structure models and calculation results are given in Fig. 14. It was found that the formation energy of the bulk material is lower than at the surface, and the energy for near S–Al in the bulk is lowest (−0.86) and the near S–Al doped at surface is the most stable (−3.54 eV). Consequently, the structural stability was enhanced by doping due to the formation of stronger Al–O bonds and the adsorption properties were improved by increasing the charge density *via* S doping.[34]

3.5.2 Density of states. To further understand the mechanism of the increase of Li^+ adsorption capacity and the dissolution resistance of Mn by anion and cation co-doping, the electronic structure including the density of states (DOS) and the charge density were investigated. The DOS of LMO and LMO-SAl are illustrated in Fig. 15a and d. The calculation results reveal that the valence band is mainly composed of Mn(d) and O(p), indicating that there is a strong interaction between Mn and O in [MnO_6]. The calculated bandgap of LMO-SAl is 0.24 eV, which are slightly lower than bare LMO (0.17 eV), indicating that the electronic conductivity was not enhanced by S and Al co-doping.

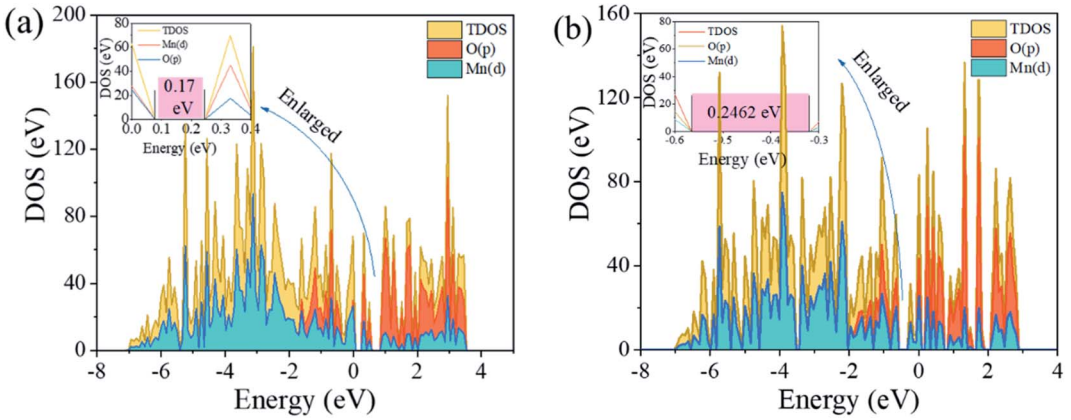

Fig. 15 Calculated density of states (DOS) for (a): un-doped LMO and (b): LMO-SAl.

4. Conclusion

With the goal of developing high performing adsorbents for Li^+ recovery from salt lake, a series of $Li_{1.6}Mn_{1.6}O_4$ (LMOs) co-doped with anions and cations were prepared, which enhanced the adsorption of Li^+ and reduced the dissolution of Mn. The adsorption capacity of LMO-SAl reached 33.7 mg g^{-1}, which is higher the bare LMO (26.1 mg g^{-1}). The Mn dissolution was reduced from 5.4% for bare LMO to 3.7% for LMO-SAl. The co-doped LMOs also possess a high selectivity for Li^+ from Lagoco Salt Lake brine containing Li^+, Na^+, K^+, Mg^{2+}, and Ca^{2+}. To further explore the adsorption and anti-dissolution improvements, DFT calculations revealed that the cause was likely charge transfer near co-doping sites, which may inform subsequent development of new materials for the recovery of Li^+ ions from mixed salt solutions.

Conflicts of interest

There are no conflicts to declare.

Acknowledgements

Financial supports from NSFC (No. U1607105, 51302280, and U20A20141), Thousand Talents Plan in Qinghai, NSF in Qinghai (2020-ZJ-901) and Youth Innovation Promotion Association, CAS (2016377).

References

1 B. Swain, Recovery and recycling of lithium: A review, *Sep. Purif. Technol.*, 2017, **172**, 388–403.
2 H. Saravaia, H. Gupta and V. Kulshrestha, Single step synthesis of a magnesium doped lithium manganese oxide ion sieve nanomaterial and a SPES/ion sieve composite membrane for the separation of lithium, *RSC Adv.*, 2016, **6**, 106980–106989.
3 L. Zhang, J. Li, L. Ji and L. Li, Separation of lithium from alkaline solutions with hydrophobic deep eutectic solvents based on beta-diketone, *J. Mol. Liq.*, 2021, **334**, 117729–117738.
4 C. Zhang, Y. Mu, W. Zhang, S. Zhao and Y. Wang, PVC-based hybrid membranes containing metal-organic frameworks for Li^+/Mg^{2+} separation, *J Membrane. Sci.*, 2020, **596**, 117724–117734.
5 F. Qian, M. Guo, Z. Qian, B. Zhao, J. Li, Z. Wu and Z. Liu, Enabling highly structure stability and adsorption performances of $Li_{1.6}Mn_{1.6}O_4$ by Al-gradient surface doping, *Sep. Purif. Technol.*, 2021, **264**, 118433–118442.
6 H. J. Hong, I. S. Park, T. Ryu, J. Ryu, B. G. Kim and K. S. Chung, Granulation of $Li_{1.33}Mn_{1.67}O_4$ (LMO) through the use of cross-linked chitosan for the effective recovery of Li^+ from seawater, *Chem. Eng. J.*, 2013, **234**, 16–22.
7 Q. H. Zhang, S. P. Li, S. Y. Sun, X. S. Yin and J. G. Yu, $LiMn_2O_4$ spinel direct synthesis and lithium ion selective adsorption, *Chem. Eng. Sci.*, 2010, **65**, 169–173.
8 F. Qian, B. Zhao, M. Guo, Z. Qian, N. Xu, Z. Wu and Z. Liu, Enhancing the Li^+ adsorption and anti-dissolution properties of $Li_{1.6}Mn_{1.6}O_4$ with Fe, Co doped, *Hydrometallurgy*, 2020, **193**, 105291–105300.
9 F. Qian, B. Zhao, M. Guo, Z. Qian, Z. Wu and Z. Liu, Trace doping by fluoride and sulfur to enhance adsorption capacity of manganese oxides for lithium recovery, *Mater. Design*, 2020, **194**, 108867–108878.
10 R. Chitrakar, Y. Makita, K. Ooi and A. Sonoda, Synthesis of iron-doped manganese oxides with an ion-sieve property: lithium adsorption from bolivian brine, *Ind. Eng. Chem. Res.*, 2014, **53**, 3682–3688.
11 D. S. Hall, R. Gauthier, A. Eldesoky, V. S. Murray and J. R. Dahn, New chemical insights into the beneficial role of Al_2O_3 cathode coatings in lithium-ion cells, *ACS Appl. Mater. Interfaces*, 2019, **11**, 14095–14100.
12 Y. Mu, C. Zhang, W. Zhang and Y. Wang, Electrochemical lithium recovery from brine with high Mg^{2+}/Li^+ ratio using mesoporous λ-MnO_2/$LiMn_2O_4$ modified 3D graphite felt electrodes, *Desalination*, 2021, **511**, 115112–115122.
13 R. Chitrakar, H. Kanoh, Y. Makita, Y. Miyai and K. Ooi, Synthesis of spinel-type lithium antimony manganese oxides and their Li^+ extraction/ion insertion reactions, *J. Mater. Chem.*, 2000, **10**, 2325–2329.
14 R. Chitrakar, Y. Makita, K. Ooi and A. Sonoda, Magnesium-doped manganese oxide with lithium ion-sieve property: lithium adsorption from salt lake brine, *B. Chem. Soc. Jpn.*, 2013, **86**, 850–855.
15 G. Cao, X. Yang, Z. Yin, Y. Lei, H. Wang and J. Li, Synthesis, adsorption properties and stability of Cr-doped lithium ion sieve in salt lake brine, *Bull. Chem. Soc. Jpn.*, 2019, **92**, 1205–1210.
16 L.-W. Ma, B.-Z. Chen, X.-C. Shi, W. Zhang and K. Zhang, Stability and Li^+ extraction/adsorption properties of $LiM_xMn_{2-x}O_4$ (M=Ni, Al, Ti; $0 \le x \le 1$) in aqueous solution, *Colloid. and Surfaces A*, 2010, **369**, 88–94.
17 J. Duan, S. Chen, A. Vasileff and S. Z. Qiao, Anion and Cation Modulation in Metal Compounds for Bifunctional Overall Water Splitting, *ACS Nano*, 2016, **10**, 8738–8745.
18 A. Gao, X. Hou, Z. Sun, S. Li, H. Li and J. Zhang, Lithium-desorption mechanism in $LiMn_2O_4$, $Li_{1.33}Mn_{1.67}O_4$, and $Li_{1.6}Mn_{1.6}O_4$ according to precisely controlled acid treatment and density functional theory calculations, *J. Mater. Chem. A*, 2019, **7**(36), 20878–20890.
19 F. Qian, B. Zhao, M. Guo, J. Li, Z. Liu and Z. Wu, K-gradient doping to stabilize spinel structure of $Li_{1.6}Mn_{1.6}O_4$ for Li^+ recovery, *Dalton Trans.*, 2020, 1–10.
20 H. Lin, X. Yu, M. Li, J. Duo, Y. Guo and T. Deng, Synthesis of Polyporous Ion-Sieve and Its Application for Selective Recovery of Lithium from Geothermal Water, *ACS Appl. Mater. Interfaces*, 2019, **11**, 26364–26372.
21 L. W. Ma, B. Z. Chen, X. C. Shi, W. Zhang and K. Zhang, Stability and Li^+ Extraction/Adsorption Properties of $LiM_xMn_{2-x}O_4$ (M=Ni, Al, Ti; $0 \le x \le 1$) in Aqueous Solution, *Colloids Surf., A*, 2010, **369**, 88–94.
22 F. Qian, B. Zhao, M. Guo, Z. Wu, W. Zhou and Z. Liu, Surface trace doping of Na enhancing structure stability and

adsorption properties of $Li_{1.6}Mn_{1.6}O_4$ for Li^+ recovery, *Sep. Purif. Technol.*, 2020, **20**, 117583–117593.

23 R. Chitrakar, H. Kanoh, Y. Miyai and K. Ooi, A new type of manganese oxide ($MnO_2 \cdot 0.5H(2)O$) derived from $Li_{1.6}Mn_{1.6}O_4$ and its lithium ion-sieve properties, *Chem. Mater.*, 2000, **12**, 3151–3157.

24 Z.-Y. Ji, M.-Y. Zhao, Y.-Y. Zhao, J. Liu, J.-L. Peng and J.-S. Yuan, Lithium extraction process on spinel-type $LiMn_2O_4$ and characterization based on the hydrolysis of sodium persulfate, *Solid State Ionics*, 2017, **301**, 116–124.

25 S. H. Ye, J. K. Bo, C. Z. Li, J. S. Cao, Q. L. Sun and Y. L. Wang, Improvement of the high-rate discharge capability of phosphate-doped spinel $LiMn_2O_4$ by a hydrothermal method, *Electrochim. Acta*, 2010, **55**, 2972–2977.

26 C. Y. Tang, K. Leung, R. T. Haasch and S. J. Dillon, $LiMn_2O_4$ surface chemistry evolution during cycling revealed by in situ auger electron spectroscopy and X-ray photoelectron spectroscopy, *ACS Appl. Mater. Interfaces*, 2017, **9**, 33968–33978.

27 S. R. Kasireddy, B. Gangaja, S. V. Nair and D. Santhanagopalan, Mn^{4+} rich surface enabled elevated temperature and full-cell cycling performance of $LiMn_2O_4$ cathode material, *Electrochim. Acta*, 2017, **250**, 359–367.

28 X. Luo, K. Zhang, J. Luo, S. Luo and J. Crittenden, Capturing lithium from wastewater using a fixed bed packed with 3-D MnO_2 ion cages, *Environ. Sci. Technol.*, 2016, **50**, 13002–13012.

29 X. Shi, D. Zhou, Z. Zhang, L. Yu, H. Xu, B. Chen and X. Yang, Synthesis and properties of $Li_{1.6}Mn_{1.6}O_4$ and its adsorption application, *Hydrometallurgy*, 2011, **110**, 99–106.

30 Z. Liu, R. Yu, Y. Dong, W. Li and B. Lv, The adsorption behavior and mechanism of Cr(VI) on 3D hierarchical α-Fe_2O_3 structures exposed by (0 0 1) and non-(0 0 1) planes, *Chem. Eng. J.*, 2017, **309**, 815–823.

31 Z. Liu, Y. Zhou, M. Guo, B. Lv, Z. Wu and W. Zhou, Experimental and theoretical investigations of Cs^+ adsorption on crown ethers modified magnetic adsorbent, *J. Hazard. Mater.*, 2019, **371**, 712–720.

32 X. Shi, D. Zhou, Z. Zhang, L. Yu, H. Xu, B. Chen and X. Yang, Synthesis and Properties of $Li_{1.6}Mn_{1.6}O_4$ and Its Adsorption Application, *Hydrometallurgy*, 2011, **110**, 99–106.

33 X. Xu, Y. Chen, P. Wan, K. Gasem, K. Wang, T. He, H. Adidharma and M. Fan, Extraction of lithium with functionalized lithium ion-sieves, *Prog. Mater. Sci.*, 2016, **84**, 276–313.

34 Q. Gan, H. He, Y. Zhu, Z. Wang, N. Qin, S. Gu, Z. Li, W. Luo and Z. Lu, Defect-Assisted Selective Surface Phosphorus Doping to Enhance Rate Capability of Titanium Dioxide for Sodium Ion Batteries, *ACS Nano*, 2019, **13**, 9247–9258.